Robust model-based detection of the lung field boundaries in portable chest radiographs supported by selective thresholding

2009 Meas. Sci. Technol. 20 104019

(http://iopscience.iop.org/0957-0233/20/10/104019)

IOP PUBLISHING MEASUREMENT SCIENCE AND TECHNOLOGY

Meas. Sci. Technol. **20** (2009) 104019 (10pp) doi:10.1088/0957-0233/20/10/104019

Robust model-based detection of the lung field boundaries in portable chest radiographs supported by selective thresholding

D K Iakovidis[1,3], M A Savelonas[1] and G Papamichalis[2]

[1] Department of Informatics and Computer Technology, Technological Educational Institute of Lamia, GR-35100 Lamia, Greece

[2] 1st Department of Thoracic Surgery, Chest Hospital of Athens 'Sotiria', Greece

E-mail: dimitris.iakovidis@ieee.org and msavelonas@ieee.org

Received 1 February 2009, in final form 26 May 2009
Published 4 September 2009
Online at stacks.iop.org/MST/20/104019

Abstract

Portable chest radiography is a valuable tool for screening patients hospitalized in intensive care, providing visual cues for diagnosis and physiological measurements. However, its practicality comes at the cost of quality, which is mainly affected by misaligned body positioning, thus increasing x-ray misinterpretation rates. This paper presents a novel methodology for the detection of the lung field boundaries in portable chest radiographs of patients with bacterial pulmonary infections. Such infections are radiographically manifested as foci of consolidations which can lead to vague or invisible lung field boundaries, difficult to distinguish even by experienced physicians. Conventional and state-of-the-art approaches address mainly stationary radiographs, whereas only a few of them cope with pulmonary infections. The proposed methodology is based on an active shape model incorporating shape prior information about the lung fields. The model is initialized by a novel technique utilizing a set of salient points detected on the peripheral anatomic structures of the lungs. A selective thresholding algorithm based on a spinal cord sampling process supports both the initialization and the evolution of the model for the detection of the lung field boundaries. The experiments show that the proposed methodology outperforms state-of-the-art approaches.

Keywords: portable chest radiography, lung, infections, active shape models, thresholding, physiological measurements

1. Introduction

The first and the most critical step in computerized analysis of chest radiographs is the detection of the lung field boundaries. Once the boundaries of the lung fields are defined, assessment of the condition of the lungs and physiological measurements can take place [1, 2]. Plain chest radiographs are usually obtained in a controlled setup where the patients are positioned in a standard way at the x-ray device. However, in the case of critically ill patients, this is not always feasible as they may be in pain or disabled. To cope with this problem, portable x-ray devices are commonly used in intensive care to obtain the radiographs from various relative distances and angles to patients immobilized in bed—not necessarily in a standard position. However, its practicality comes at the cost of quality mainly because of misaligned body positioning during image acquisition [3]. Consequently, such radiographs are more difficult to read and subject to a higher misinterpretation rate.

The detection of the lung field boundaries becomes even more difficult in the presence of bacterial pulmonary infections. The most common radiographic manifestation of such infections is foci of consolidations [4]. These are

[3] Author to whom any correspondence should be addressed.

visible as bright shadows interfering with the interior lung intensities and can lead to weak lung field boundaries, difficult to distinguish even by experienced physicians. Therefore, a computational approach that would robustly detect the boundaries of the lung fields would be an asset to the medical community.

Since the beginning of the 1960s, a variety of computational approaches to the detection of the lung field boundaries in plain chest radiographs have been proposed. These include rule-based methodologies [6–12], neural network, Markov random fields and other pattern classification approaches [1, 13, 14], active contour models [15], active shape and active appearance models [16] and graph cuts [17]. The studies [6–11] indicate that the detection performance of most rule-based methodologies can degrade if the quality of the radiograph is poor or if the positioning of the patient deviates from the standard. Recently, a rule-based approach coping with the issue of positioning has been proposed in [12]. This approach is unsupervised and defines a set of salient control points around the lung fields. The salient point detection process is supported by a selective thresholding algorithm that cuts off image intensities based on local intensity histograms sampled from the spinal cord. The detected points are then intuitively interpolated by Bézier curves [18]. The preliminary results presented indicate its suitability for portable radiography, its robustness to the presence of consolidations and its advantage against the graph cuts approach [17]. A drawback of this methodology is that it may produce implausible shapes especially if parts of the lung fields are excluded from the radiograph.

Supervised state-of-the-art approaches that have provided excellent solutions to the detection of the lung field boundaries include active shape and active appearance models [1, 5, 16]. Active shape models (ASMs) [19] represent the shape of an image region by the principal components of landmark point vectors, whereas the grey-level appearance of that region is limited to its border and consists of the normalized first derivative of the intensity profiles centred at each landmark that run perpendicular to the region's contour. The evolution of the model involves the minimization of the distance between the true and the modelled first derivative profiles of the region. Active appearance models (AAMs) [20] have been proposed as an alternative to ASMs. In AAMs, a combined principal component analysis of the landmarks and pixel values inside the region is made facilitating the generation of plausible instances of both geometry and texture. The evolution of the model is steered by the difference between the true pixel values and the modelled pixel values within the region. The comparative advantage of the ASMs and the AAMs over pattern classification and rule-based approaches is that they incorporate *a priori* shape information, thus they are capable of producing more plausible shapes in their output. However, their dependence on local image derivatives makes them sensitive to fitting weak boundaries thus increasing the likelihood of the contour to leak through these boundaries. Experimental results of the application of an ASM for the detection of the lung field boundaries in the presence of a bacterial infection have been presented in [5], where the results reported indicate the prevalence of such errors. Although ASMs have not yet been applied explicitly on portable radiographs, their shape-constrained deformability makes them a competent candidate.

In this paper, we propose a novel methodology for lung field boundary detection suitable for portable chest radiographs of patients with bacterial pulmonary infections. The proposed methodology is based on the ASM approach which is initialized and enhanced by techniques from [12], in order to limit contour leaking in the presence of lung consolidations. The initialization of the ASM is determined by a novel technique utilizing a set of salient points detected on the peripheral anatomic structures of the lungs. A selective thresholding algorithm based on a spinal cord sampling process supports both the initialization and the evolution of the model for the detection of the lung field boundaries. This methodology provides robustness to the lung field deformation in the presence of weak boundaries and produces plausible shapes even if parts of the lung fields are excluded from the radiograph. Moreover, as in [12] but unlike the conventional approaches, the lung field regions overlapped by the heart are not excluded since abnormalities due to bacterial infections may be present, even behind the heart [4].

The remainder of this paper consists of three sections. Section 2 describes the proposed methodology. Section 3 presents the results of its experimental evaluation in comparison with relevant state-of-the-art approaches. The conclusions derived from this study are summarized in the last section, where perspectives for future research are also provided.

2. Methodology

The proposed methodology assumes that (a) the patient's body may not necessarily be aligned with the portable x-ray device, since he/she may be immobilized in bed and (b) the spinal cord lies roughly somewhere in the middle of the radiograph, considering that both the patient's lungs are examined.

Let I be a new chest radiograph of size $N \times M$ pixels. The detection of the lung field boundaries is realized in three phases:

(1) salient points detection;
(2) selective thresholding;
(3) ASM-based image segmentation.

In the first phase, a set of points indicating two regions bounded by the outer ribcage and the spinal cord is detected. This set of points is used as input to the next phases. In the second phase, the chest radiograph I is processed so that image regions irrelevant to the problem investigated are subtracted from it. In the last phase, the processed image is used to guide the evolution of the ASM, which is modified so as to achieve robust and accurate detection of the lung fields. The three phases of the proposed methodology are described in the following subsections.

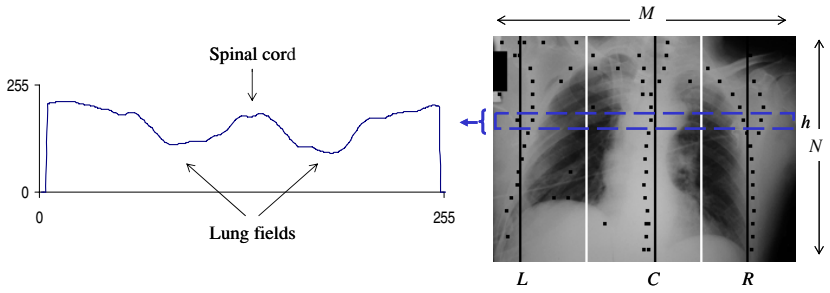

Figure 1. Salient point detection. The image is sampled with rectangular windows as that indicated with dashed borders on the right. An example profile extracted from this window is illustrated on the left. The detected maxima indicated as black points on the right. The black vertical lines indicate the midlines of the central, left and right columns. The white vertical lines are located at $[L + (C - L)/2]$ and $[R + (R - C)/2]$.

2.1. Salient point detection

The peripheral anatomic structures to the lungs, such as the spinal cord and the ribcage, remain unaffected by the presence of a pulmonary bacterial infection. Based on this consideration the first phase of the proposed methodology aims to detect a set of salient points that fall approximately on outer ribcage and the spinal cord, indicating two regions, each of which encloses a lung field.

Radiograph I is uniformly sampled from top to bottom with s_h non-overlapping rectangular windows of $h \times M$, pixels, where $h < N$ (figure 1). For each sample an average horizontal profile, i.e. the average grey level of its rows, per column, is estimated. Radiographic image profiles have been proved valuable in several radiographic image analysis tasks [5–8, 11] as they provide a simple though effective means to navigate through a radiograph by using only one-dimensional information and elementary signal processing techniques. The proposed methodology utilizes horizontal profiles of consecutive image samples in order to obtain spatial instances of the radiograph from which the spinal cord and the ribcage boundaries are detectable even if the patient is bent. This sampling approach does not consider standard lung field positioning as the approaches mentioned in [5–8, 11]. An example profile is illustrated in figure 1. The two valleys around the central peak correspond to the lung fields, whereas the peaks after these valleys correspond to the ribcage boundaries. Each profile is smoothed by following a moving average approach that facilitates noise insensitivity. The local maxima detected for each profile are illustrated as black points on the radiograph of figure 1. The localization of the maxima remains practically unaffected by the presence of consolidations, since their density, and therefore their intensity, is generally lower than the density of the spinal cord and of the ribcage [4, 21].

In the following, possibly relevant maxima are selected and classified into three sets: (a) spinal cord points, (b) points of the left side of the ribcage and (c) points of the right side of the ribcage. To this direction, s_v non-overlapping rectangular windows of $N \times w$, $w < M$, pixels uniformly sample the radiograph from left to right and the average intensity of each sample is estimated. Considering a chest radiograph that displays both the patient's lungs, it is assumed that the spinal cord lies roughly somewhere in the middle of the image. This is implemented by assigning as candidate spinal cord points those bilaterally closer to the column with the maximum average intensity within columns $[M/4]$ and $[3M/4]$. This column will be referred to as the *central column* C.

Similarly, a *left column* L and a *right column* R are determined as the columns with the maximum average intensity between columns 0 and $[M/4]$, and between columns $[3M/4]$ and M, respectively. Considering the relative positions of the lung fields with respect to the spinal cord [7], the points closest to the left side of column $[L + (C - L)/2]$ are selected as candidate points belonging to the left side of the ribcage and the points closest to the right side of column $[R + (R - C)/2]$ are selected as candidate points belonging to the right side of the ribcage.

The salient point detection algorithm is implemented as follows:

Step 1. Detect local maxima of horizontal profiles:

- Acquire s_h consecutive non-overlapping rectangular samples of $h \times M$, $h < N$ pixels from the whole image.
- For each of s_h samples
  - calculate its average horizontal profile;
  - detect the local maxima of each profile.

Step 2. Detect a central, a left and a right column:

- Acquire s_v non-overlapping rectangular samples of $N \times w$, $w < M$ pixels from the whole image.
- For each of s_v samples
  - calculate the average intensity.
- Set as central column C the midline of the sample with the maximum average intensity between columns $M/2 - M/4$ and $M/2 + M/4$.
- Set as left column L the midline of the sample with the maximum average intensity between columns 0 and $M/2 - M/4$.
- Set as right column R the midline of the sample with the maximum average intensity between columns $M/2 + M/4$ and $M - 1$.

Step 3. Classify the detected local maxima to the spinal cord, and to the outer left and right boundaries of the left and the right lung field, respectively.

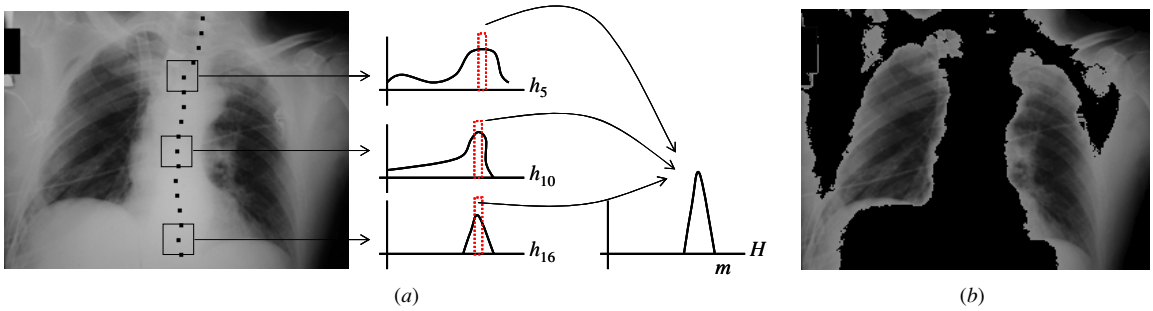

Figure 2. Selective thresholding. (*a*) Histograms h_i, $i = 1, \ldots, s_h$ are calculated from samples acquired at the spinal cord points. The histogram peaks indicated with dashes are accumulated to H. (*b*) The output of the selective thresholding algorithm.

- For each of s_h samples:
  - Set the local maxima closest to C as spinal cord points.
  - Set the local maxima closest to the left side of column $L + (C - L)/2$ as points of the outer left boundary of the left lung field.
  - Set the local maxima closest to the right side of column $R + (R - C)/2$ as points of the outer right boundary of the right lung field.

2.2. Selective thresholding

The second phase applies the selective thresholding algorithm, preliminarily described in [12], in order to subtract regions that do not belong to the lung fields, from the chest radiograph. This algorithm is based on the fact that every anatomic structure visible in the radiograph is characterized by a set of intensities depicting its density [21].

The selective thresholding algorithm begins with sampling the spinal cord at the points detected in the previous step of this methodology. Sampling is performed with square windows centred at each point (figure 2). From each sample the highest histogram peak along with its neighbouring histogram components are selected. The selected components from all samples are accumulated in a new single histogram H. The non-zero components of that histogram will correspond to the most prevalent intensities of the spinal cord, the heart and other anatomic structures that overlap the spinal cord.

By setting these intensities to zero, a significant part of, or even the whole image regions corresponding to the anatomic structures that overlap the spinal cord are subtracted from I. Moreover, since many other structures in the radiograph, except for the lung fields, are of similar densities to those across the spinal cord, they are expected to have similar intensity distributions. For example, the spinal cord consists of bone tissue similar to the clavicles. Therefore, a part of these structures will also be subtracted from I.

Further subtraction of irrelevant image regions is performed by setting all the intensities of I that are higher than the maximum intensity m of H, to zero. This operation subtracts from I image regions that are unlikely to belong to the lung fields since the spinal cord is generally brighter that both normal lung parenchyma and consolidations. Such regions may include dense objects used for patient's monitoring or support.

The selective thresholding algorithm is implemented as follows:

Step 1. Sample the radiograph across spinal cord:

- For each of s_h salient points detected on the spinal cord
  - acquire a square image sample of x^2 pixels.
- For each image sample $i = 1, \ldots, s_h$:
  - calculate its intensity histogram h_i,
  - select a set of histogram components ph_i centred at its highest peak.

Step 2. Accumulate the values ph_i from all samples into a single histogram H.
Step 3. Find the last non-zero component m of H.
Step 4. Generate an output image $T(I)$ from I as follows:

- set the intensities of I that correspond to the non-zero components of H, to zero;
- set the intensities of I that are larger than m, to zero.

The results of this algorithm can improve if the spinal cord points are populated by interpolation before the application of step 1. This is due to the increase of the samples acquired, which leads to a more representative statistical distribution of intensities in H.

2.3. ASM-based image segmentation

The shape of a lung field can be described by n landmark points $(x_1,y_1), \ldots, (x_n, y_n)$ forming a shape vector $\mathbf{x} = (x_1, y_1, \ldots, x_n, y_n)^T$. The ASM approach [19] applies principal component analysis (PCA) to build a shape model from a set of training shape vectors of ground truth lung field boundaries in different chest radiographs.

Let $\bar{\mathbf{x}}$ denote the mean of N training shape vectors.

$$\bar{\mathbf{x}} = \frac{1}{N}\sum_{i=1}^{N} x_i. \tag{1}$$

The covariance matrix of the shape vectors is

$$\mathbf{C_x} = \frac{1}{N}\sum_{i=1}^{N} (\mathbf{x}_i - \bar{\mathbf{x}})(\mathbf{x}_i - \bar{\mathbf{x}})^{\mathrm{T}} \tag{2}$$

from which t eigenvectors ϕ_i, $i = 1, \ldots, t$ corresponding to the largest eigenvalues λ_i, $i = 1, \ldots, t$, are estimated. The value

of t is determined as the smallest t for which the following inequality holds [5]

$$\sum_{i=1}^{t} \lambda_i \geqslant f_v \sum_{i=1}^{2n} \lambda_i \tag{3}$$

where f_v is the desired percentage of the shape variation to be represented by the t principal eigenvectors. The eigenvectors form the matrix

$$\Phi = (\phi_1 | \, \phi_2 | \cdots | \phi_t) \tag{4}$$

which is used for the approximation of a shape $\mathbf{x}$ in

$$\mathbf{x} = \bar{\mathbf{x}} + \Phi \cdot \mathbf{b}_\mathbf{x}, \tag{5}$$

where $\mathbf{b}_\mathbf{x}$ holds the shape parameters. Since Φ is orthogonal the shape parameters can be estimated from equation (5)

$$\mathbf{b}_\mathbf{x} = \Phi^{\mathrm{T}}(\mathbf{x} - \bar{\mathbf{x}}). \tag{6}$$

In addition to the shape, the ASM models also the local appearance of the image region around each landmark. The local appearance is represented by the normalized first derivatives of image intensity profiles sampled around each landmark, perpendicular to the contour. The derivatives are used instead of image intensities in order to reduce the effects of global intensity changes. Considering that the intensity profiles of $\mathbf{x}$ are $\mathbf{g}_i = (g_{i1}, g_{i2}, \ldots, g_{i2k+1})^{\mathrm{T}}$, $k > 0$, centred around each landmark $i = 1, \ldots, n$, the normalized first derivatives $\mathbf{d}_i = (d_{i1}, d_{i2}, \ldots, d_{i2k})^{\mathrm{T}}$ are estimated by

$$d_{il} = \frac{g_{il+1} - g_{il}}{\sum_{j=1}^{2k} |g_{ij+1} - g_{ij}|}, \qquad l = 1, \ldots, 2k. \tag{7}$$

The local appearance model is represented by the mean $\bar{\mathbf{d}}_i$ and the covariance matrix $\mathbf{C}_{\mathbf{d}i}$ of the normalized first derivatives, estimated for any landmark $i = 1, \ldots, n$ over the N training shapes.

The trained ASM is applied on a new chest radiograph after proper initialization and evolves to detect the lung field boundaries.

2.3.1. Initialization. The application of the ASM [19] on a new chest radiograph requires that the initial position, the rotation and the scale of the mean shape of each lung field are defined. To overcome this limitation, we propose a novel approach for the initialization of the ASM. The proposed initialization approach aims to provide an initial model that falls close to the target lung field boundaries.

Primarily, the outer left and right salient points detected in the first phase of our methodology are interpolated by Bézier curves [18] and connected, so as to segment I into two regions (figure 3(*a*)). We have considered the Bézier curves because they feature robustness to outliers [12]. These curves are intuitively controlled by the salient points, in the sense that they are attracted by the internal control points, without necessarily passing through them. The segmented image is binarized so that the pixel values under the curve are equal to 1, and the pixel values over the curve are equal to 0. This binary image is denoted as $B_I(I)$ (figure 3(*b*)).

Secondly, a binary instance $B_T(I)$ of $T(I)$ is obtained by setting its non-zero pixel values to 1 (figure 3(*c*)). The two

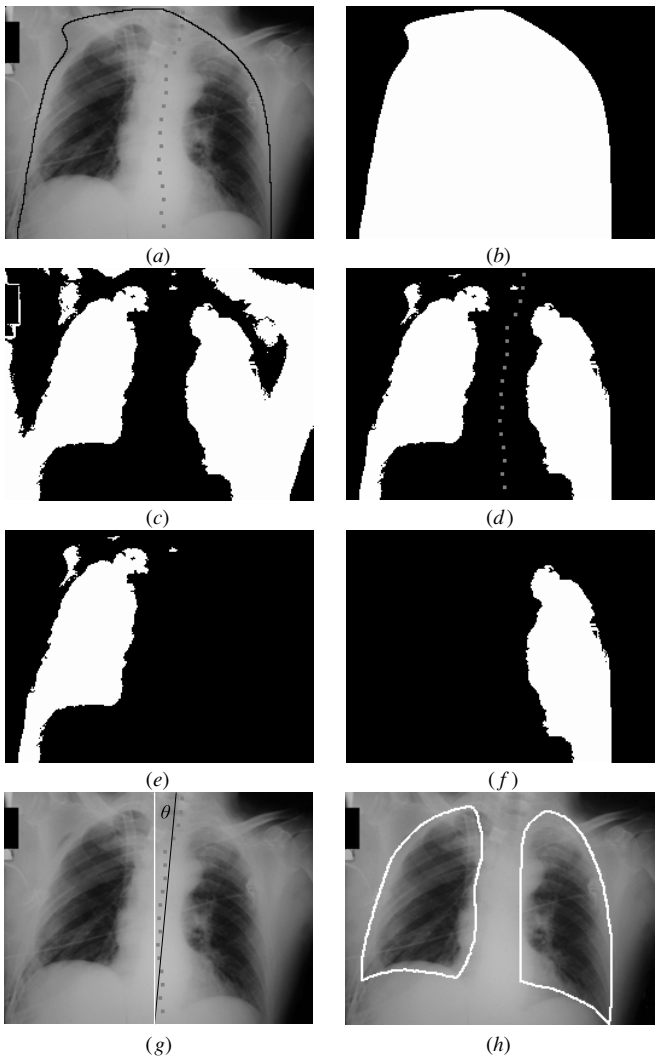

Figure 3. Proposed ASM initialization. (*a*) Interpolation of the outer left and right salient points detected in the first phase of our methodology; (*b*) the binary image $B_I(I)$; (*c*) the binary instance $B_T(I)$ of $T(I)$ (illustrated in figure 2(*b*)); (*d*) the result of $B_{IT}(I) = B_I(I) \wedge B_T(I)$, the points in the middle indicate the spinal cord points dividing the image into two parts, $B^L_{IT}(I)$ and $B^R_{IT}(I)$; (*e*) left part of $B^L_{IT}(I)$; (*f*) right part of $B^R_{IT}(I)$; (*g*) the rotation angle θ between the (black) line produced by linear regression and the (white) vertical axis of the image; (*h*) initial contours $\bar{\mathbf{x}}^i$, $i = L$, R, obtained from the data set used in the experiments.

binary images $B_I(I)$ and $B_T(I)$ are then combined with the logical 'and' operator to produce a new binary image $B_{IT}(I)$ (figure 3(*d*)), which can be considered as a rough mask for the two lung fields. This mask is further divided by the spinal cord points into two parts: a left part $B^L_{IT}(I)$ (figure 3(*e*)) and a right part $B^R_{IT}(I)$ (figure 3(*f*)), corresponding to each of the two lung fields. The centre of mass of each part is chosen for the positioning of the centre of mass of the mean shape of each lung field. The centre of mass is estimated by the two first-order geometric moments of the binary image [24]. The rotation of both mean shapes is determined by the angle θ between the line obtained with linear regression from the spinal cord points and the vertical axis of the image [25] (figure 3(*g*)). Given a fixed position and the rotation angle

of the mean shape of the left and the right lung field, the corresponding lung field model is iteratively scaled up until it reaches a maximum overlap with the shapes of the non-zero regions of $B^L_{IT}(I)$ and $B^R_{IT}(I)$, respectively (figure 3(*h*)). The *overlap* ω between the areas of two shapes; a_1 and a_2, is defined by the ratio [26]

$$\omega = \frac{a_1 \cap a_2}{a_1 \cup a_2}. \tag{8}$$

The translation, rotation and scaling of the shape model are realized by the application of the following well-known geometric transformation on each of its landmarks (x, y) [23]

$$\begin{pmatrix} x' \\ y' \end{pmatrix} = \begin{pmatrix} \Delta x \\ \Delta y \end{pmatrix} + \psi \cdot \begin{pmatrix} \cos\theta & -\sin\theta \\ \sin\theta & \cos\theta \end{pmatrix} \begin{pmatrix} x \\ y \end{pmatrix}, \tag{9}$$

where Δx and Δy correspond to the horizontal and vertical translations of the shape's centre of mass, θ is the rotation angle of the spinal cord and ψ is the scaling factor of the shape.

The proposed ASM initialization algorithm is implemented as follows:

Step 1. Generate rough binary masks $B^L_{IT}(I)$, $B^R_{IT}(I)$ for each lung field:

- calculate $B_{IT}(I) = B_I(I) \wedge B_T(I)$.
- divide $B_{IT}(I)$ into two parts based on the spinal cord points and generate images $B^L_{IT}(I)$ and $B^R_{IT}(I)$ from each part, such that $B_{IT}(I) = B^L_{IT}(I) \vee B^R_{IT}(I)$.

Step 2. For each $B^i_{IT}(I)$, $i = L, R$:

- Calculate its centre of mass o^i by its first-order geometric moments.

Step 3. Calculate the rotation angle θ of the spinal cord by linear regression of the spinal cord points.

Step 4. Initialize lung field models:
For each model $\mathbf{x}^i = \bar{\mathbf{x}}^i + \Phi^i \cdot \mathbf{b}^i_{\mathbf{x}}$, $i = L, R$:

- Set scale $\psi^i = \psi_{\text{initial}}$.
- Set initial overlap $\omega^i_{\max} = 0$.
- Repeat the following until maximum ω^i is found.
  - Transform $\bar{\mathbf{x}}^i$ using o^i, θ, ψ^i in equation (9).
  - Estimate the overlap ω^i of $\bar{\mathbf{x}}^i$ with the non-zero area of $B^i_{IT}(I)$.
  - $\psi^i = \psi^i + \psi_{\text{step}}$
- Set model parameters $\mathbf{b}^i_{\mathbf{x}} = \mathbf{0}$.

2.3.2. Evolution. The initialized ASM evolves according to a simple iterative scheme [19]. Each landmark can move along a direction perpendicular to the contour by s positions on either side of the contour, evaluating $2s + 1$ positions, in total. The new position (x'_i, y'_i) of each landmark $i = 1, \ldots, n$, on the search direction, is determined as the one minimizing the Mahalanobis distance

$$\mu(\mathbf{d}'_{ij}) = (\mathbf{d}'_{ij} - \bar{\mathbf{d}}_i)^{\mathrm{T}} \mathbf{C}^{-1}_{\mathbf{d}i} (\mathbf{d}'_{ij} - \bar{\mathbf{d}}_i), \tag{10}$$

where $\mathbf{d}'_{ij}$ is a vector of normalized first derivatives estimated from the $2s + 1$ pixel intensity profile centred at each of the possible new landmark positions (x'_{ij}, y'_{ij}), $i = 1, \ldots, n$, $j = 1, \ldots, 2s + 1$. After all the landmarks are updated, the shape model is fitted to the new landmarks. The ASM evolves until a proportion p_{close} of landmarks ends up within $s/2$ of its previous position, or until a number of $M_{\max}$ iterations is reached. The convergence of this algorithm improves by repeating this process with intensity profiles sampled at multiple resolutions $R_{\max}$, considering respective local appearance models of multiresolution image pyramids [22, 23].

Figure 4. Detection of the lung fields after initialization with the contours illustrated in figure 3(*h*). The model for each lung field has been built with the data set used in the experiments.

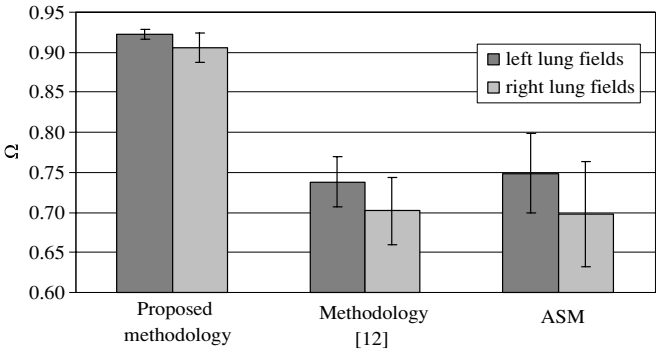

Figure 5. Graphical representation of the results presented in table 1.

The evolution of the ASM on a new chest radiograph is likely to get affected by the presence of irrelevant anatomic structures or external objects. Consequently, the lung field boundaries may be missed and contour leaking may be observed, especially if the boundaries are weakly defined. To alleviate this problem we introduce limitations to the evolution of the ASM by imposing constraints derived from $T(I)$.

The proposed approach for the evolution of the ASM considers the possibility that the non-zero pixels of $T(I)$ correspond to the lung fields and prohibit the contour to move towards them in I. This way it is less likely for the ASM contour to leak inside the lung fields. The initialization of the model as described in the previous subsection and the incorporation of multiresolution local appearance models help the algorithm to avoid trapping into irrelevant regions. Moreover, the *a priori* shape information included in the ASM helps the algorithm to achieve a plausible delineation of the lung fields even if part of them remains joint with their surroundings, or artefacts are present, in $T(I)$.

The proposed ASM evolution algorithm is implemented as follows:

Step 1. Update landmark positions:

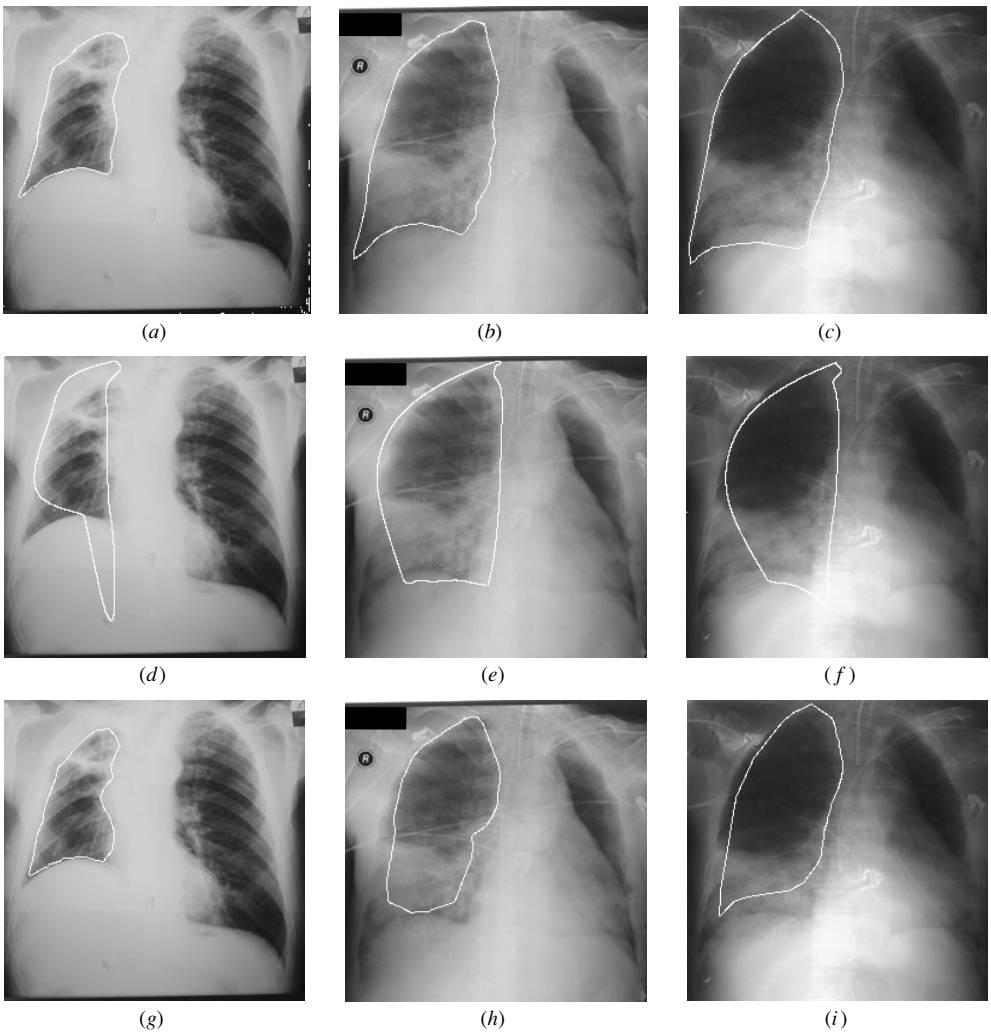

Figure 6. Delineations of the right lung fields obtained by the application of the proposed methodology (*a*)–(*c*), the methodology proposed in [12] (*d*)–(*f*) and the original ASM (*g*)–(*i*), on the same x-ray images.

- For each possible new landmark position (x'_{ij}, y'_{ij}), $i = 1, \ldots, n$, $j = 1, \ldots, 2s + 1$:
  - Calculate a profile of normalized first derivatives $\mathbf{d}'_{ij} = (d_{ij1}, d_{ij2}, \ldots, d_{ij2k})^{\mathrm{T}}$ on I, centred at this landmark position perpendicular to the contour.
  - Calculate the Mahalanobis distance $\mu(\mathbf{d}'_{ij})$.
  - From all $\mathbf{d}'_{ij}$, such that $T(I(x'_{ij}, y'_{ij})) = 0$, find $\mu_{\min}(\mathbf{d}'_i) = \min_{j=1,\ldots,2s+1}(\mu(\mathbf{d}'_{ij}))$.
  - $(x'_i, y'_i) = (x'_{ij}, y'_{ij})$ is the new position of landmark i.

Step 2. Fit the current shape model to the updated landmarks:

- Set $x' = (x'_1, y'_1, \ldots, x'_n, y'_n)^T$.
- Calculate the new model parameters for $\mathbf{x}'$ from equation (6).
- Constrain each component $|b_l| < c\sqrt{\lambda_l}$ of $\mathbf{b}_{\mathbf{x}'}$, $c > 0$, $l = 1, \ldots, t$, to ensure plausible shapes.

Step 3. Repeat steps 1–3 until a proportion of p_{close} of points ends up within $s/2$ of the previous positions, or $M_{\max}$ iterations are reached.

Step 4. Move to the next resolution level.

Step 5. Repeat steps 1–5 until the finest resolution level $R_{\max}$ is reached.

3. Experimental evaluation

The effectiveness of the proposed approach was evaluated on a set of 107 anonymous chest radiographs obtained with a portable x-ray device from patients with pulmonary bacterial infections, manifested as consolidations. The patients were hospitalized in an intensive care unit of the Chest Hospital of Athens 'Sotiria'. This is a challenging data set since the majority of the radiographs are misaligned and in some cases parts of the lung fields are even excluded from the radiograph, while a variety of external objects used for patients' monitoring and support are also present.

All radiographs used in the experiments were digitized at 8 bits and have been downscaled to fit a 256 × 256 pixel bounding box. For each model parameter, a fixed setting was selected that yielded good performance, after initial pilot experiments. A shape model explaining 98% of the variance ($f_v = 0.98$) was constructed. Other settings include three

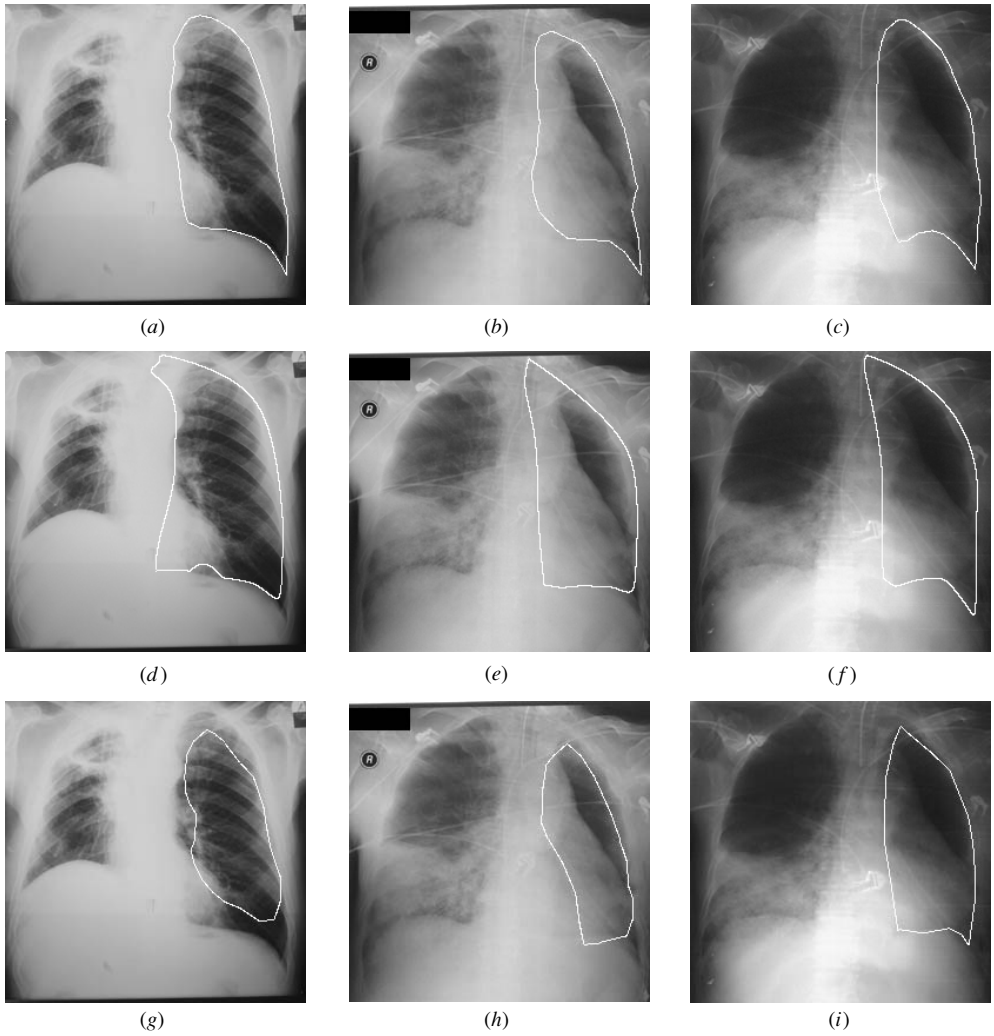

Figure 7. Delineations of the left lung fields obtained by the application of the proposed methodology (*a*)–(*c*), the methodology proposed in [12] (*d*)–(*f*), and the original ASM (*g*)–(*i*), on the same x-ray images.

levels of resolution ($R_{\max} = 3$), 30 iterations per resolution level ($M_{\max} = 30$), profiles of length five ($s = 2$). When fitting the shape model to the displaced landmarks, each mode was constrained within two times the standard deviation. Additional values of parameters associated with the sizes used for the salient point detection and selective thresholding include $w = h = 9$ and $x = 32$, as these are supported by the preliminary experiments performed in [12].

The performance of the proposed methodology was assessed in terms of Ω, a widely accepted measure of accuracy for binary segmentation tasks [16]:

$$\Omega = \frac{\mathrm{TP}}{\mathrm{TP} + \mathrm{FP} + \mathrm{FN}}, \tag{11}$$

where TP stands for true positive (the area classified as lung by both the proposed methodology and the expert), FP for false positive (area classified as background by the expert and as lung by the proposed methodology) and FN for false negative (area classified as lung by the expert and as background by the proposed methodology). $\Omega = 1$ holds for a perfect result and $\Omega = 0$ holds if there is no overlap at all between the detected and true lung fields. This measure more closely reflects the idea of a good segmentation than the average distance between the true and detected landmark locations, because the latter is not sensitive to shifts of the landmarks along the contour [27]. In addition, Ω is a more suitable measure of segmentation performance than the accuracy used in [12], since the latter counts TN pixels as correctly detected, providing deceptively high results in cases of relatively small target objects.

A leave-one-out cross-validation scheme was employed for the evaluation of the supervised methodologies, involving a total of 107 experiments. In each experiment, 106 different images sampled from the data set were used for training and 1 image not belonging to the training set, for testing. Table 1 presents the mean values of Ω obtained for each of the lung fields by using the proposed methodology, the original ASM and the preliminary unsupervised methodology proposed in [12]. These results are also graphically illustrated in figure 5. It can be noted that the proposed methodology outperforms both previous methodologies. In addition, it exhibits a considerably lower variance in the values of Ω, which indicates robust behaviour over the various unfavourable conditions included in the utilized data set. The performance of the original ASM is comparable to the performance of the methodology proposed

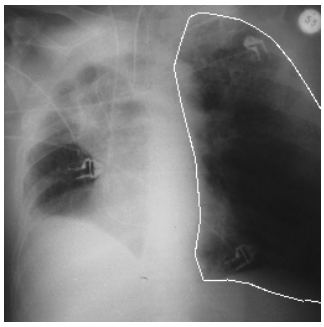

Figure 8. Indicative delineation obtained by the proposed methodology in a case of partially excluded lung field.

Table 1. Mean values and standard deviation (std) of Ω obtained for the detection of the lung fields using the proposed and state-of-the-art methodologies.

Lung field	Left		Right	
	Mean	Std	Mean	Std
ASM supported by selective thresholding	90.6	2.7	92.3	1.2
Methodology proposed in [12]	70.2	8.4	73.8	6.3
ASM	69.8	13.2	74.9	9.8

in [12] although the latter is unsupervised. This could be attributed to the diversity of the radiographs in the problem investigated. However, although theoretically the performance of a supervised methodology such as the original ASM has the potential to increase if more, representative, training samples are provided, it is usually impractical to find such samples.

In order to point out the advantages of the proposed methodology we have selected three indicative radiographs from our data set and perform a qualitative comparison of the three methodologies. The lung field delineations obtained by their application on the left and right lung fields are illustrated in figures 6 and 7, respectively.

Figures 6 and 7 show that the unsupervised methodology proposed in [12] may result in implausible shapes. This is more evident on the right lung fields, especially in the case illustrated in figure 6(*d*), where the algorithm is misled by edges originating from artefacts below the right lung field. On the other hand, the original ASM could not prevent leaking of the contour into the lung fields, especially in cases where the boundaries of the lung fields are weakly defined (figures 6(*h*) and (*i*), 7(*h*) and (*i*)). Moreover, it occasionally excludes the region of the heart overlapping the right field boundaries (figure 7(*g*), (*h*)).

The proposed methodology robustly achieves accurate delineations, even in the presence of weakly defined boundaries (figures 6(*b*) and (*c*), 7(*b*) and (*c*)), whereas it does not exclude the region of the heart, where abnormalities due to bacterial infections can also be present (figures 7(*a*)–(*c*)). In addition, the *a priori* shape information included in the proposed methodology allows the algorithm to achieve a plausible delineation of the lung fields even if artefacts (figure 6(*a*)) or dense external objects used for patient's monitoring and support (figures 6(*b*), (*c*)) are present. Moreover, the proposed methodology is not affected by the misalignment of the utilized images and it is capable of producing plausible delineations even if part of the lung fields is not included in the radiograph (figure 8)

4. Conclusions and future research perspectives

A novel methodology for the detection of the lung field boundaries in chest radiographs was presented and experimentally evaluated. It has been developed to cope with weak and deformed lung field boundaries, which is a prevalent situation in real clinical setups, especially in intensive care. It has been inspired by two state-of-the-art approaches [12, 16], which have been effectively combined into a single, improved, model-based methodology featuring both robustness and accuracy.

The results from its experimental evaluation of the proposed method on a challenging data set of portable radiographs obtained from critically ill patients with bacterial pulmonary infections lead to the following conclusions:

- it is capable of detecting the lung field boundaries in portable radiographs with high accuracy regardless of the patients' positioning, thus it provides an excellent means for lung area or volume measurements [2];
- it generally remains unaffected by the presence of abnormalities originating from bacterial pulmonary infections;
- it outperforms the methodology proposed in [12] by incorporating shape information about the lung fields, since it produces plausible output even if parts of the lung fields are excluded from the radiograph;
- it outperforms the original ASM approach by incorporating the selective thresholding algorithm so as to limit contour leaking;
- it is resistant to the presence of dense external objects used for patient's monitoring and support;
- as in [12] but unlike current approaches, it does not exclude the overlapping region of the heart from the lung fields, where abnormalities due to bacterial infections can also be present.

The proposed method can be used for the measurement of the area of the segmented lung fields. For example, comparing the areas of the two lung fields could provide useful information about the presence of atelectasis [3], whereas in [2] it has been shown that area measurements of the lung fields can be used for the estimation of the lung volumes. Moreover, the extraction of measures quantifying the intensity and the texture of the segmented regions could provide useful information about the presence and the extent of lung consolidations.

Future research perspectives include further improvement of the proposed methodology by incorporating additional features in the formulation of the model, analysis of the detected lung fields for automatic assessment of pulmonary bacterial infections and measurement of physiological parameters. The evaluation of the proposed scheme in

the presence of other kinds of abnormalities including abnormalities attached to the lung field boundaries is also a challenging perspective. This research will contribute to the development of a multimodal data mining system for adverse events detection, which will be capable of co-evaluating radiographic findings of patients with bacterial infections [28].

Acknowledgment

This work was supported in part by the European Commission's Seventh Framework Information Society Technologies (IST) Programme, Unit ICT for Health, project DEBUGIT (no. 217139).

References

[1] Ginneken B V, Romeny B T H and Viergever M A 2001 Computer-aided diagnosis in chest radiography: a survey *IEEE Trans. Med. Imaging* **20** 1228–41

[2] Ries A L, Clausen J L and Friedman P J 1979 Measurement of lung volumes from supine portable chest radiographs *J. Appl. Phys.* **47** 1332–5

[3] Bongard F S and Sue D Y 2002 *Current Critical Care Diagnosis & Treatment* 2nd edn (New York: McGraw-Hill)

[4] Müller N L, Franquet T, Lee K S, Isabela C and Silva S 2006 *Imaging of Pulmonary Infections* (Baltimore, MD: Williams & Wilkins)

[5] Ginneken B V, Katsuragawa S, Romeny B T H, Doi K and Viergever M A 2002 Automatic detection of abnormalities in chest radiographs using local texture analysis *IEEE Trans. Med. Imaging* **21** 139–49

[6] Meyers P H, Nice H C, Becker C M, Nettleton N J, Sweeney J W and Meckstroht G R 1964 Automated computer analysis of radiolographic images *Radiology* **13** 1029–34

[7] Xu X-W and Doi K 1995 Image feature analysis for computer aided diagnosis: accurate determination of the ribcage boundary in chest radiographs *Med. Phys.* **22** 617–26

[8] Duryea J and Boone J 1995 A fully automatic algorithm for the segmentation of lung fields in digital chest radiographic images *Med. Phys.* **22** 183–91

[9] Luo H, Gaborski R and Acharya R 2000 Automatic segmentation of lung regions in chest radiographs: a model guided approach *Proc. Int. Conf. Image Processing (ICIP 2000)* vol 2 pp 483–6

[10] Ginneken B V and Romeny B T H 2000 Automatic segmentation of lung fields in chest radiographs *Med. Phys.* **27** 2445–55

[11] Iglesias I, Tahoces P G, Souto M, Martinez de Alegria A, Lado M J and Vidal J J 2004 Lung segmentation on postero-anterior digital chest radiographs using active contours *Lecture Notes in Computer Science* vol 3138 ed A Fred *et al* (Berlin: Springer) pp 538–46

[12] Iakovidis D K and Papamichalis G 2008 Automatic segmentation of the lung fields in portable chest radiographs based on bézier interpolation of salient control points *Proc. IEEE Int. Conf. on Imaging Systems and Techniques (Chania, Greece)* pp 82–7

[13] McNitt-Gray M F, Huang H J and Sayre J W 1995 Feature selection in the pattern classification problem of digital chest radiograph segmentation *IEEE Trans. Med. Imaging* **14** 537–47

[14] Vittitoe N, Vargas-Voracek R and Floyd C Jr 1999 Markov random field modeling in posteroanterior chest radiograph segmentation *Med. Phys.* **26** 1670–7

[15] Coppini G, Diciotti S, Falchini M, Villari N and Valli G 2003 Neural networks for computer-aided diagnosis: detection of lung nodules in chest radiograms *IEEE Trans. Inf. Technol. Biomed.* **7** 344–57

[16] Ginneken B V, Stegmann M B and Loog M 2006 Segmentation of anatomical structures in chest radiographs using supervised methods: a comparative study on a public database *Med. Image Anal.* **10** 19–40

[17] Chen S, Cao L, Liu J and Tang X 2006 Automatic segmentation of lung fields from radiographic images of SARS patients using a new graph cuts algorithm *Proc. Int. Conf. Pattern Recognition (ICPR 2006)* vol 1 pp 271–4

[18] Bartels R H, Beatty J C and Barsky B A 1998 Bézier curves *An Introduction to Splines for Use in Computer Graphics and Geometric Modelling* (San Francisco, CA: Morgan Kaufmann) chapter 10, pp 211–45

[19] Cootes T, Taylor C, Cooper D and Graham J 1995 Active shape models—their training and application *Comput. Vis. Image Underst.* **61** 38–59

[20] Cootes T F, Edwards G J and Taylor C J 2001 Active appearance models *IEEE Trans. Pattern Anal. Mach. Intell.* **23** 681–5

[21] Novelline R A 1997 *Squires's Fundamentals of Radiology* (Cambridge, MA: Harvard University Press)

[22] Cootes T 2000 An introduction to active shape models *Image Processing and Analysis* ed R Baldock and J Graham (Oxford: Oxford University Press) chapter 7, pp 223–48

[23] Gonzalez R C and Woods R E 2008 *Digital Image Processing* 3rd edn (Upper Saddle River, NJ: Prentice-Hall)

[24] Prokop R J and Reeves A P 1992 A survey of moment-based techniques for unoccluded object representation and recognition *CVGIP: Graphical Models and Image Processing* vol 54 (Amsterdam: Elsevier) pp 438–60

[25] Montgomery D C, Peck E A and Vining G 2003 *Introduction to Linear Regression Analysis* 3rd edn (New York: Wiley)

[26] Crum W R, Camara O and Hill L G 2006 Generalized overlap measures for evaluation and validation in medical image analysis *IEEE Trans. Med. Imaging* **25** 1451–61

[27] Ginneken B V, Frangi A F, Staal J J, Romeny B T H and Viergever M 2002 Active shape model segmentation with optimal features *IEEE Trans. Med. Imaging* **21** 924–33

[28] Lovis C, Colaert D and Stroetmann V N 2008 DebugIT for patient safety—improving the treatment with antibiotics through multimedia data mining of heterogeneous clinical data *Stud. Health Technol. Inform.* **136** 641–6